Open Research Online

The Open University's repository of research publications
and other research outputs

In situ observation of strain and phase transformation in plastically deformed 301 austenitic stainless steel

Journal Item

oro.open.ac.uk

In situ observation of strain and phase transformation in plastically deformed 301 austenitic stainless steel

Yadunandan B. Das[1], Alexander N. Forsey[1], Thomas H. Simm[2], Karen M. Perkins[2], Michael E. Fitzpatrick[3], Salih Gungor[1], Richard J. Moat[1*]

1. *Materials Engineering, Open University, Walton Hall, Milton Keynes MK7 6AA, UK*

2. *Institute of Structural Materials, Swansea University, Bay Campus, Swansea SA1 8EN, UK*

3. *Faculty of Engineering and Computing, Coventry University, Priory Street, Coventry CV1 5FB, UK*

*Corresponding author. Tel.: +441908332134. E-mail address: <u>richard.moat@open.ac.uk</u>

Abstract

To inform the design of superior transformation-induced plasticity (TRIP) steels, it is important to understand what happens at the microstructural length scales. In this study, strain-induced martensitic transformation is studied by *in situ* digital image correlation (DIC) in a scanning electron microscope. Digital image correlation at submicron length scales enables mapping of transformation strains with high confidence. These are correlated with electron backscatter diffraction (EBSD) prior to and post the deformation process to get a comprehensive understanding of the strain-induced transformation mechanism. The results are compared with mathematical models for enhanced prediction of strain-induced martensitic phase transformation.

Keywords: TRIP steel, DIC, EBSD, Martensite, SEM, MTEX

1. Introduction

The need for improvement of crash-worthiness of automobile structural components without increasing their overall weight has led to the development of high-strength steels. High strength in steel can be achieved in a number of ways [1]. One class of high-strength steels of current interest are those that derive their strength from the formation of hard solid-state transformation products in the form of hard constituent martensite phase [2]–[5]. The advantage of this is that it also gives rise to exceptional ductility. Martensitic transformations are solid-state diffusionless transformations that have been extensively investigated over the past century[3], [6]–[8], yet still continue to intrigue the research community [2], [9], [10]. Zackay *et al.* were the first to exploit martensitic transformations to enhance ductility of steels, coining the now well-known term TRansformation Induced Plasticity (TRIP) steels [11].

The high strength and improved ductility of TRIP steels is due to a combination of the hard martensite phase in the soft austenite matrix, analogous to a hard-particle-reinforced composite [12]. The solid-state solution hardening of carbon in iron and the very high dislocation density obtained from the rapid diffusionless martensitic transformation are further exploited in the strengthening process. Extensive literature can be found on martensite's influence on the properties of TRIP type steels, such as the correlation between martensite fraction and strength [2], [13], [14], martensite fraction and ductility [10], and deformation and transformation kinetics [15]–[18]. Also, one particular area of conjecture was the origin of exceptional ductility in TRIP type steels, with many authors attributing it to transformation strain [19], a theory mathematically disproven by Bhadeshia in [12] and to some extent experimentally corroborated by some of the current authors in [2] and shown to be closely related to composite theory. It is reasonable to assume that for better understanding of the strengthening mechanisms that lead to the exceptional strength and ductility of TRIP steels, there needs to be thorough investigation of local stresses and strains observed in the vicinity of the transformation product. It is as a result of these stress and strain fields around transformation sites that dislocation movement and localised plasticity are resisted [20], [21].

The local stress and strain state around a single martensite region is influenced by many factors, however those believed to be of most significance are: the orientation of the martensite forming and the extent to which the parent grain has slipped. The orientation of the forming martensite directly influences the transformation strain. In this manuscript we report an analysis of the local strain occurring during the strain induced martensite transformations and variant selection based on the Patel and Cohen theory [22] as reported in [23].

In TRIP material the formation of martensite is mechanically induced. Essentially, metastable FCC (face-centred cubic) austenite is transformed into martensite by the addition of strain energy. In commercially interesting alloys such as those reported in [2], small regions of austenite are retained by heat treatment and then transformed mechanically to form a ferrite matrix with small martensite regions. These commercially interesting alloys are far too complex, both in terms of microstructure and phase makeup, for the purpose of gaining an understanding and ultimately predicting the local strains and crystallography of TRIP martensite. Therefore, the material reported here is a meta-stable, virtually 100% austenitic, type 301 stainless steel. This material is known to transform to martensite under room temperature deformation [24], [25] and due to the almost fully austenitic starting microstructure, offers an opportunity to isolate newly forming martensite for analysis.

For each austenite grain there are 24 possible crystallographic variants of martensite that can form. For each of these variants the resulting strain and stress local to the martensite plate will be different.

This will have a direct influence on the material's ability to resist non-uniform deformation and reduce the desirable properties of high strength and exceptional ductility. Kundu *et al*. [23], [26], [27], using crystallographic data from the austenite phase as input parameters, compared the martensite variants predicted and experimentally measured. They assumed that the interaction of applied stress with the shape deformation associated with the martensitic transformation determined the favourable variants formed. The interaction energy *U* between the applied stress and martensite was as suggested by Patel and Cohen [22].

$$U = \sigma_N\delta + \tau s$$

Where σ_N is stress component normal to the habit plane of the martensite, τ is the shear stress resolved on the habit plane in the direction of shear, and δ and s are the respective normal and shear strains associated with transformation. This interaction leads to formation of a transformation texture. If this is the case for TRIP steels in general it will mean that with knowledge of the starting austenite texture, the orientations of the martensite expected to form can be calculated, and although not within the scope of this work, the mechanical properties can be predicted.

In this manuscript, the deformation at the microstructural length scale of 301 stainless steel deformed plastically to induce martensitic transformation is reported using EBSD and an *in situ*, high-resolution digital image correlation (HRDIC) technique. These techniques have been proven in [28]–[33] as very useful tools to develop understanding of microstructural length scale deformation. Combination of the HRDIC and EBSD give a comprehensive insight into material behaviour at different stages of the deformation process. Discussion here is focussed on strain-induced martensite formation on the active {111} slip planes and how the material constraints within a grain and its surrounding affect the overall transformation mechanisms. The aim is to understand plasticity at the microstructural length scale, and ultimately apply these data sets as input data for improving reliability of existing material models.

2. Experimental

This section describes the experimental techniques used for the measurement of the local strain during strain-induced martensitic transformations. It starts by giving an introduction to the material used in the tests. This is followed by parameters used for EBSD on the same set of grains prior to and post the deformation process. Finally, the *in situ* micro-mechanical tests for HRDIC data acquisition and treatment for data acquired within a scanning electron microscope is explained. These data are used to map plasticity due to slip and martensitic phase transformation, within individual austenite grains**.**

2.1. Material

The material studied for this work is a 301 grade austenitic stainless steel. This material is nominally fully austenitic (FCC crystal structure), with good oxidation and corrosion resistance properties and is used for decorative and structural applications. As mentioned earlier, this material has been selected because it has nearly 100% austenitic starting material. This reduces the complications of analysis introduced by other BCC type phases such as ferrite and bainite, which are often present in TRIP steels. At room temperature this material readily transforms into martensite on application of stress [25], [34]. The material was received in a fully annealed condition with a grain size of 15-20 μm and relatively free from preferred orientation (see figure 1) with the chemical composition given in Table 1.

Table 1 the chemical composition of a 301 austenitic stainless steel

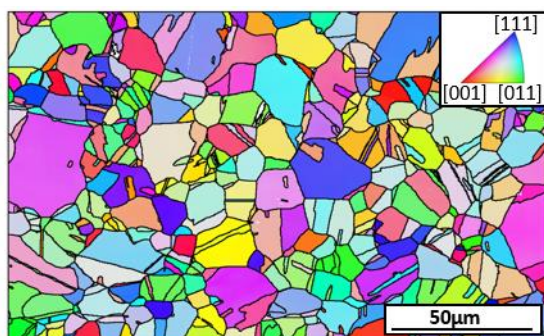| Fe	C	Si	Mn	P	S	Cr	Ni	Cu	Mo
Bal.	0.001	0.48	1.057	0.043	0.001	16.98	7.12	0.381	0.311

Figure 1: EBSD orientation map of the as received material having more than 99% austenite.

A 301 stainless steel sheet with a nominal thickness of 1.6 mm was machined into flat dog-bone shaped specimen having 20 mm gauge length and 3 mm width (see figure 2). Figure 2 schematically shows the testing regime. Stages I, II and V are explained in greater detail in the following 3 sections. During stage IV, the specimen was incrementally strained using a strain rate of 4×10^{-4} from 2 to 10 % strain with 2 % strain increments.
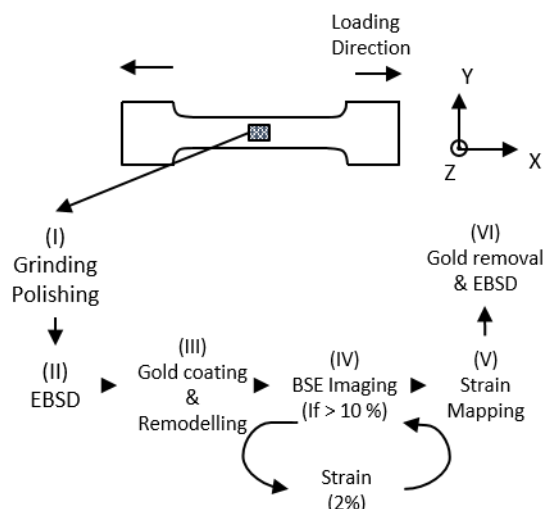
Figure 2: Schematic flowchart of experimental procedure.

The specimen was strained using *an in situ* 4.5 kN ADMET mini-tensile testing machine, inside a Zeiss Supra 55VP field emission gun scanning electron microscope (FEG SEM). At each macroscopic strain value, the test was interrupted to capture three backscattered electron (BSE) images at two different magnifications to be used for DIC analysis. The region of interest (ROI) for the high magnification images was contained within the lower magnification images. The parameters used for image capture are shown in table 2.

Table 2 SEM Imaging parameters

Image	Imaging Mode	Accelerating Voltage	Working distance	Magnification	Image size (pixels)		Spatial resolution (nm)
Low mag	BSE	20	11.6 mm	2000X	2048 1536	x	92
Hi mag	BSE	20	11.6 mm	5000X	2048 1536	x	37

2.2. EBSD

Prior to any further analysis or testing, the specimen was metallographically prepared by grinding and polishing, removing approximately 85 μm of material from the sample surface, and electro-polished using an electrolyte solution of 85% ethanol, 10% 2-butoxyethanol and 5% water (branded as Struers A21). During stage II (see figure 2), EBSD was performed prior to deforming the sample with a step-size of 0.2 μm. Greater than 99% volume fraction of austenite was observed (figure 1). Stage V involves very careful processing of the sample to remove the gold nano-particles from the surface preserving the microstructural features beneath. Here the specimen was polished using a 0.25 μm diamond paste solution for less than a minute followed by finally polishing up to 10 minutes using OP-S to improve

EBSD indexing, similar to the method used by Di Gioacchino *et al.* [32]. The EBSD measurement is then performed with a step size of 0.15 μm to identify the thin martensite plates formed during the deformation process, which will be discussed in the results section. The analysis of the EBSD data was conducted using the Matlab toolbox MTEX [35].
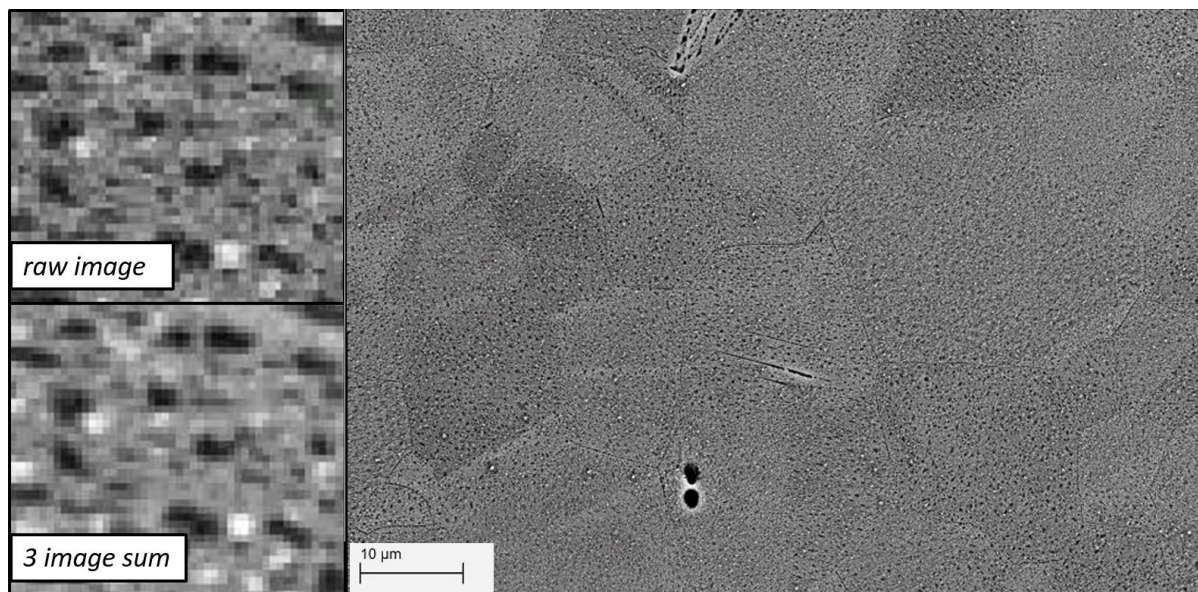

Figure 3: Backscatter image of gold remodelled speckle pattern used for digital image correlation. Raw image shows speckle pattern of a single image, 3-image sum is combination of three images actually used for correlation.

2.3. HRDIC data collection

After the initial EBSD scanning, the test specimen is coated with a thin > 50 nm film of gold using a K575X gold sputter coater. The surface with the gold layer is then held at 350 °C for 90 minutes in a humid atmosphere. This causes the gold layer to re-distribute into a fine speckle pattern (see figure 3). This method has been developed by Gioacchino *et al.* [28], and used by the same authors in their recent work [32] providing sub-pixel accuracy in strain measurements from SEM imaging. As a consequence of being far apart in the periodic table, the gold particles give an excellent contrast with the steel substrate in the BSE imaging mode. Moreover, the BSE mode is less sensitive to changes in topography throughout the straining process, which is critical for 2D digital image correlation (DIC).

2.4. HRDIC data treatment

Digital image correlation is a computational technique that tracks small regions throughout the deformation process. These regions on the surface are tracked throughout the series of digital images, producing a displacement vector. If this is performed at positions across the entire image then a vector field is produced. If the displacement of the sample occurs in the image plane, then this vector field will describe the displacement of the imaged sample. This vector field can then be differentiated to calculate strain difference in the sample between the two images. In addition to the assumption that

the surface is moving in plane, there is also the implicit assumption that the pixels are square. This assumption is easily satisfied when using a standard camera sensor, but when using an SEM to produce the images this becomes more difficult to ensure, as described in the following paragraphs. For this reason, sets of three images were taken at each strain step so that any inconsistencies can be reduced by image summation.

Raster errors in images obtained by SEM may cause the violation of the square pixel assumption required in DIC analysis and leads to pseudo-strain in calculations. To alleviate this error, each set of three images, taken at a single strain step, was shift-corrected to sub-pixel accuracy by taking a DIC (in DaVis software using an FFT-based algorithm) measurement of the relative shifts for each image for a central 128×128 pixel region. The images were shifted to sub-pixel accuracy using bi-cubic spline interpolation and then summed together (see figure 3). As well as reducing the raster error by improving the regularity of the pixel sample points, this step increases the effective bit depth of the images and improves the quantum efficiency of the imaging process so that the image stability is increased.

The DIC analysis of BSE images was carried out using commercial software DaVis 8.2 [36]. This software uses the least-squares approach to iteratively solve the sum of squared differences (SSD) correlation function [37]. The algorithm initially calculates the displacement of a specified seed point in the image via the Lucas-Kanade method [38] using the implementation of Bouguet [39]. Once the seed point displacement is established, a "region grow" approach is then used assuming displacement continuity to limit the search area. The user specific parameters for the DIC calculation are presented in table 3.

Strain was calculated from the DIC displacement vectors using Matlab code that fits a plane to a square region containing 9 vectors: a "strain window" [40]. Strain is calculated for every vector position, by overlapping the strain windows, and is done separately for the x and y displacement fields. The gradients of the two planes, calculated from the x and y displacement fields, are taken as the average strain tensor for that vector position. By calculating strain in this way no further smoothing is required so the size of the smallest strain feature that can be resolved can be clearly established (i.e. the size of the strain window plus the size of the DIC subregion, a total of 26 pixels in this case). This method also has the advantage that strain is calculated at the same point for all parts of the strain tensor. However, in this case this makes little difference as the strain result is linearly interpolated onto the EBSD measurement points for plotting grain boundaries.

In this manuscript, the average strain in a grain is calculated in a similar manner to the local strain. In this case displacement vectors for a single grain are fitted to a plane. An outlier filter is then applied

to remove any displacement vectors that are more than 3 standard deviations from the plane. The filtered data is fitted a second time to calculate the average strain for the grain. A sliding strain window containing 9 vectors (3 × 3) was used for this work.

Table 3 DIC Parameters used for displacement vector calculation

Subregion size	Step size	Pyramid Levels	Epsilon	Correlation threshold	Threshold confidence margin	Subregion weighting	Sub-pixel interpolation
11×11 pixels	5 pixels	1	0.01	0.2 pixels	0.01	Round Gaussian	Bi-cubic spline

3. Results

Figure 4 shows high-resolution EBSD orientation maps before and after the strain-induced martensitic phase transformation. Figure 4(a) is the pre-strained EBSD grain boundary map of the as-received 301 austenitic stainless steel. It does not have any strain-induced martensite present and has austenite volume fraction greater than 99%. Figure 4 (b) is the post deformation EBSD grain boundary map showing strain-induced martensite locations within the same set of grains at 10% applied strain.

In this figure the orientation relationship between the parent austenite (γ) grain and the product martensite (α') plate used is that of Kurdjumov-Sachs (K-S) [41], where $(111)_\gamma$ is parallel to $(011)_{\alpha'}$, and $[011]_\gamma$ is parallel to $[111]_{\alpha'}$. However, it is now known that the true orientation relationship between γ/α' is irrational [42]–[44], reported as $(111)_\gamma$ parallel to $(0.012886\ 0.981915\ 0.978457)_{\alpha'}$, and the $[110]_\gamma$ direction parallel $[0.927033\ 1.055684\ -1.071623]_{\alpha'}$ [44]. Still the K-S orientation relation is found to be a good approximation. In figure 4 (b), each variant of strain-induced martensite plates is coloured distinctly and the grains labelled 1 and 2 are analysed in the following sections. Since only the martensite variant most favourable to the direction of the applied stress nucleates [27], post-straining EBSD results (figure 4b) will help in identifying the conditions for martensitic transformations, when combined with the strain maps obtained with DIC analysis. The dominance of variants 5 and 6 is interesting and may be due to the driving force from either chemical or mechanical origins being higher for these variants [26].
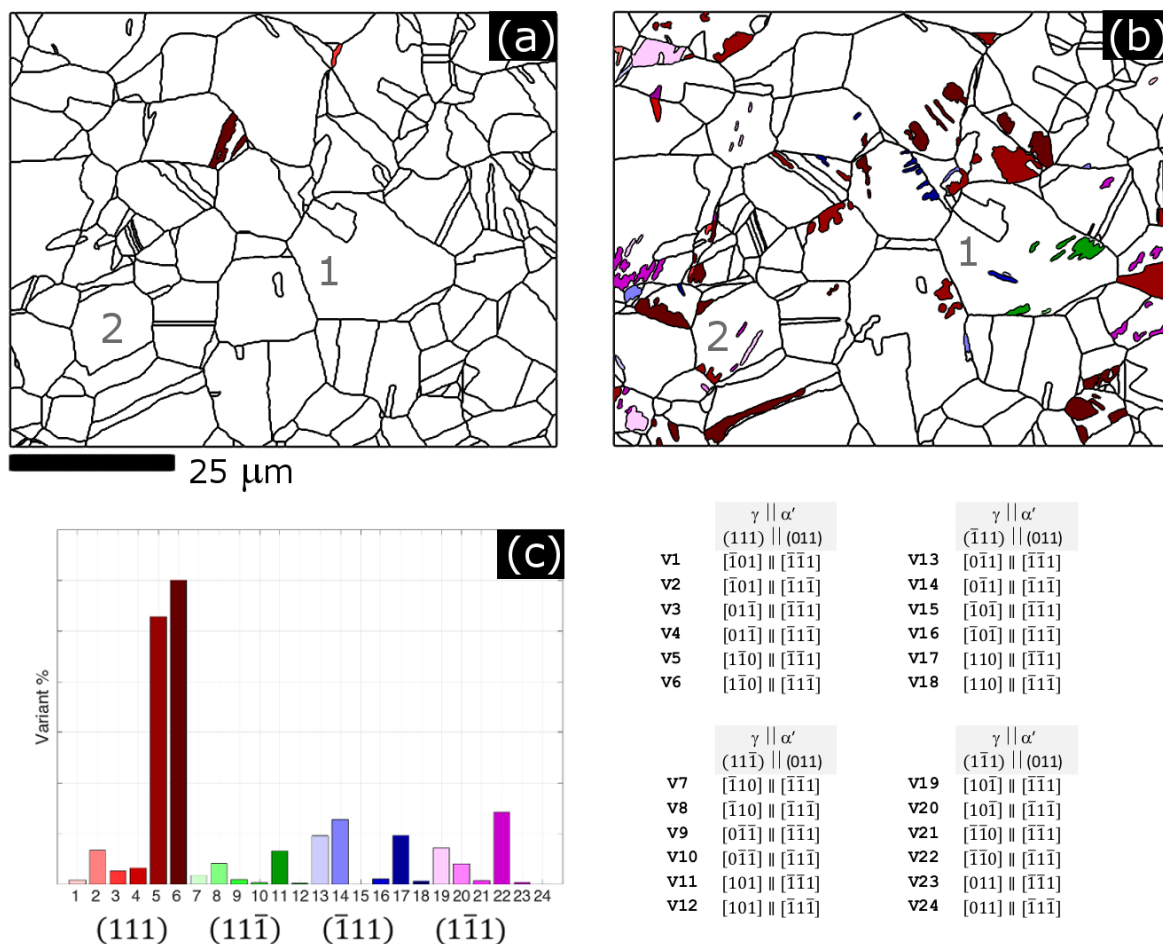
Figure 4: EBSD orientation maps of strain-induced martensitic phase transformation in the same set of grains. (a) Prior to straining having more than 99% austenite, and (b) after 10% applied strain in horizontal direction. A histogram of the frequency of different variants (by number of individual martensite grains using the lower magnification EBSD scan) is shown in (c). The details of the 24 K-S variants and the planes and directions that are parallel in the austenite and martensite are displayed. The martensite variants are coloured based on which of these 24 variants they represent.

Figure 5 illustrates the low resolution DIC strain maps overlaid over the pre-strained EBSD grain boundary map. Figures 5 (a) & (b) are the ε_{xx} strain maps at 5 and 10 % strain respectively; they clearly show the heterogeneous nature of strain accommodation in the different grains. At 10 % global strain, some grains are experiencing close to 20 % strain whilst there are nearby grains exhibiting little or no strain. We have developed a Matlab graphical user interface (GUI) for combining the EBSD and DIC data sets which uses the MTEX toolbox [35]. Details of the GUI, dbsd and dice, including capabilities and applications [45] will be published soon. The toolbox enables partitioning of DIC data with respect to individual grains calculated from EBSD grain boundary measurements. To get a representative average strain measurement, the strain outliers observed within grains are removed, however the high strains close to some grain boundaries are taken into account (figure 5(d)). Thus average ε_{xx} within individual austenite grains can be plotted (figure 5 (d) showing data for a macro strain of 10%). This allows for the strain distribution for each individual grain to be measured for each strain increment, which enabled the determination of the average ε_{xx} distribution within the different grains, at each

strain increment (figure 5 (c)). The histogram plot (figure 5(c)) shows the distribution of average strain within grains as the global strain increases (figure 5 (c)), providing a useful indication of how strain heterogeneity develops during deformation. It is observed that application of strain does not simply shift the histogram plot to the right, but it is accompanied by a change in shape of the profile.
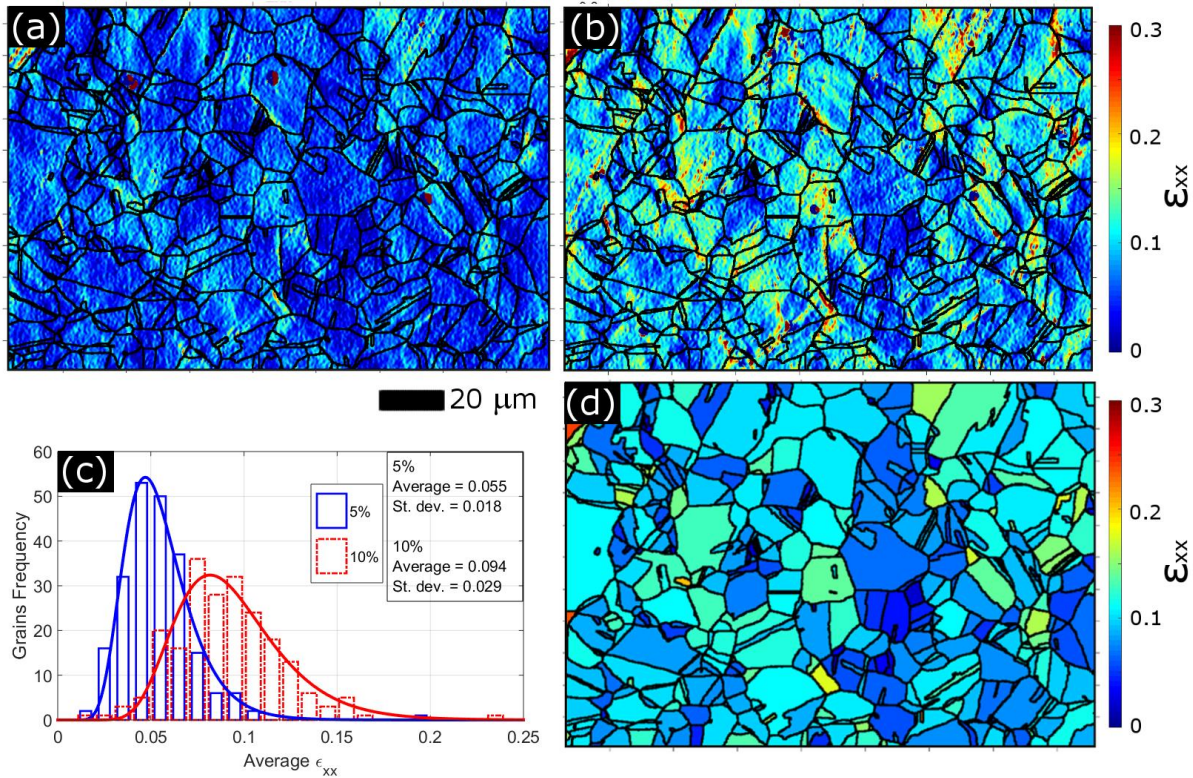

Figure 5: Low magnification strain maps overlaid with EBSD grain boundary map, showing the heterogeneous nature of strain accommodation within individual grains. (a) & (b) show ε_{xx} at 5% and 10% strain respectively. (c) Histogram plot of ε_{xx} at 5% and 10% macroscopic global strain values. (d) Map of the average ε_{xx} within grains at 10% strain used for producing (c).

To obtain greater resolution in strain, a fraction of the area was analysed at a magnification of 5000X. Figure 6 shows the HRDIC maximum shear strain map at 10 % elongation. This shear strain map is overlaid on the post-strain EBSD map of austenite grain boundary, and strain induced martensite phase boundary. In this material slip occurs on the {111} slip-lines and these are visible as shear bands that are a few microns thick. These shear bands occur at about ±45° to the loading direction, and along the direction of maximum resolved shear stress. It can be seen that on deforming the material, that

the strain-induced martensite forms and is parallel to these {111} slip planes.
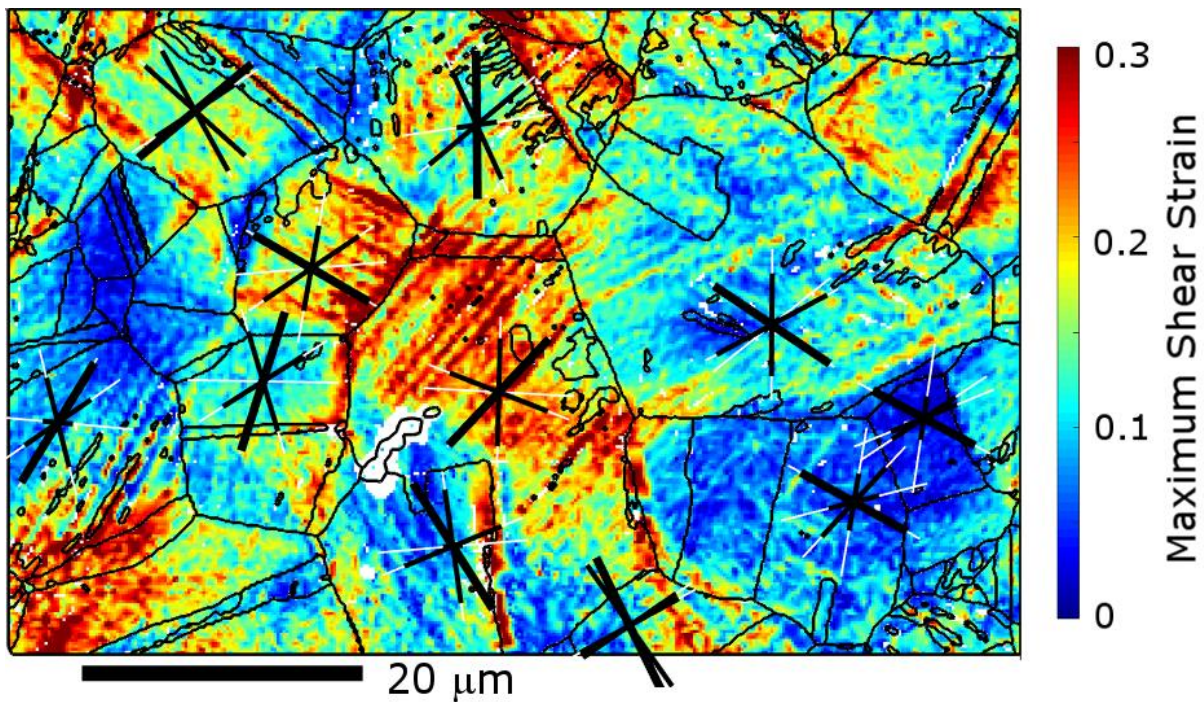

Figure 6: High magnification maximum shear strain maps overlaid on EBSD grain boundary map at 10% strain. The EBSD grain boundary map has phase transformation boundaries as well. The lines represent the different {111} slip traces; the length of the black lines is proportional to the Schmid factor and the plane with the highest Schmid factor is thicker.

4. Discussion

Acquisition of the images was performed *in situ* to eliminate the possibility of transformation or plasticity owing to back-stresses [46], which builds up during the unloading stage. It is worth noting here, that in preliminary studies of this material, higher fractions of transformation product were observed in samples that had undergone unloading cycles compared to those strained directly to the same final macro strain. Moreover, optimal contrast and resolution in BSE images is obtained at low working distance, however owing to the bulkiness of the *in situ* equipment it was not possible to obtain a working distance lower than 11.5 mm.

Due to the necessity of *in situ* testing and the higher working distance the resolution was limited compared to that obtained by Di Gioacchino *et al.* [32]. However, by performing additional processing the quality of the strain results were improved. Averaging of SEM images increased the number of vectors the DIC obtained from a given set of data. Moreover, introducing this step also reduced the number of vectors being removed at the grain averaging stage, indicating fewer spurious vectors. This indicates that there is significant benefit from taking multiple images at each increment of these quasi-static tests, with little detriment to the test efficacy or duration. From the comparison of a single image to the summed image in figure 3, it is evident that the summing process reduces the high-spatial-frequency stochastic noise present in the single images. Summing the images both reduces the effect

of the image noise, and increases the effective contrast of the speckles by summing the sensitivity depth of the images (see figure 3). This approach also mitigates the effect of step changes in e-beam position during the scanning process, as the step positions are random [47]. This dramatically improves the consistency of strains measured perpendicular to the scanning direction (the y direction in this case).

Due to two different magnifications of imaging being used on the same region, a compromise in speckle pattern size was required. The speckle pattern size was optimised for the low magnification images, where the gold remodelled surface produced a speckle size of approximately 2 pixels, which is optimal for DIC [37]. In the high-resolution images speckle size is compromised, but sufficient speckle detail was still found to enable DIC to work successfully at a similar sub-region size. The gold-remodelled surface, imaged using BSE, was found to contain sufficient detail to allow DIC to be performed over a range of length-scales and so reducing the requirement for extensive speckle optimisation investigations.

Strain localisation is observed within some grains and more evidently at certain grain boundaries. This is mainly caused by the incompatibility between grains, since they would rotate in different ways if no boundary was present [32]. However, there can be secondary effects such as the build-up or transfer of dislocations at grain boundaries (see figure 5 (a) & (b)) [48]. The low magnification data allow for a larger number of grains to be collected and provide a more representative sample of the bulk, improving the reliability of microstructural plasticity models such as the Taylor model or crystal plasticity finite element model. However, at this magnification it is difficult to resolve the strain owing to individual slip planes. This is possibly due to a small grain size of the material and lower magnification (2000X) used in these measurements compared to the higher magnification measurements at (5000X) as shown in figure 6.

The plastic deformation observed in these tests shows a periodic and discontinuous variation in shear strain. This creates regularly-spaced micro shear bands which are similar to but sharper than that observed in aluminium [49], in duplex steel [30], Fe-Cr alloy [50], but less than those measured in austenitic stainless steel [32]. The characteristic of these bands is that they form in groups and are a few microns apart from each other (see Figure 6 and 8). At higher strain values most of these shear bands become more intense. As the deformation progresses new bands form at the boundary of the existing ones. The heterogeneous nature of plastic deformation is evident from the start of the uniaxial tensile straining in all the high-resolution strain maps as shown in figure 5.

At early stages in the deformation process, plasticity does not seem to be due to the martensitic phase transformation and is possibly due to slip occurring in the material. However, martensite adds to total

plasticity and only occurs at higher global strain values at the shear band intersections, grain boundaries, or from other nucleation sites [51]. A limitation in the approach used here is that it has not been possible to separate the strains associated with slip and martensitic transformation. This could be improved if the gaps between strain increments was reduced or if the formation of the martensite could be observed, which is not possible because of the gold coating. However, these changes are impractical for the current test.
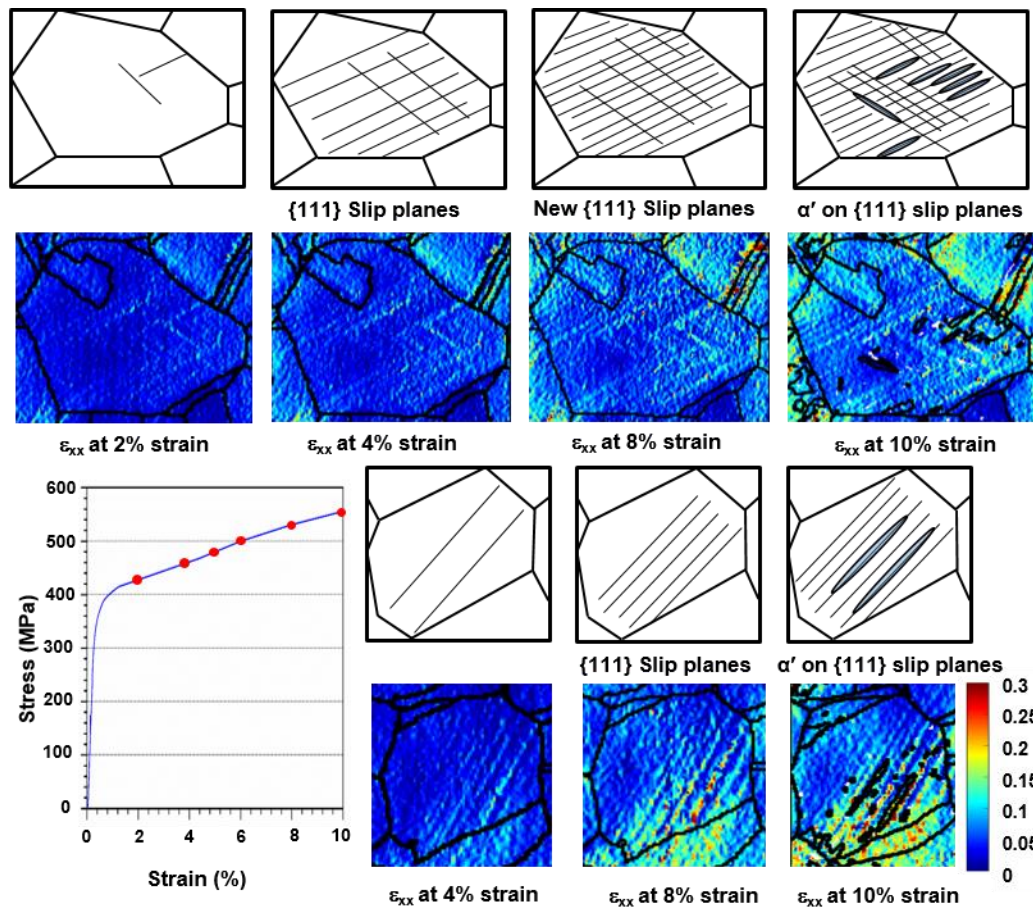

Figure 7: Mechanisms for martensitic phase transformation in fully austenitic grains. Grain 1 (top) and grain 2 (bottom) are shown with the corresponding DIC strain maps, made at various strain increments represented by red dots on the stress strain curve.

Figure 7 explains the two-step nature of the martensitic phase transformation mechanisms at room temperature for Grains 1 and 2 (refer to figure 4). Grain 1 shows two active slip systems and four martensite variants; whilst in grain 2, a single dominant slip system and three unique martensite variants are found (see figure 8). In Grain 1 there are two {111} slip planes which appear to dominate the deformation process (the green and blue lines approximately equal length), both activated when the critically-resolved shear stress is reached for that slip plane (see Figure 7 - grain 1). Other slip systems may be active, however, they do not seem to be as localised along their slip plane as the dominant ones do: that is why no additional slip lines appear in either the DIC and EBSD data sets.

Initially, when the stress exceeds the critically-resolved shear stress threshold, plasticity occurs due to shear band formation on the {111} slip planes of the austenite grains [34]. Even at relatively lower strain values of ~ 2 % strain a second slip system may be activated. Intersection of the slip/shear bands within these highly strained grains leads to potential nucleation sites for martensitic transformation [51]. The grain now contains significant overlapping of stacking faults and if further strained, these martensite (α') nucleation sites become activated leading to α' transformation [34]. In Grain 2 (Figure 7 – grain 2), only one {111} slip system is activated upon straining of the austenite grain (the pink slip plane in Figure 8 is dominant). Here, additional straining of the grain leads to activating γ to α' on the very same shear bands, where the potential nucleation site may be a region with a high density and overlapping of stacking faults. The specimen was only strained to 10 % strain, at which a small fraction (~10 %) of austenite transformed into martensite.
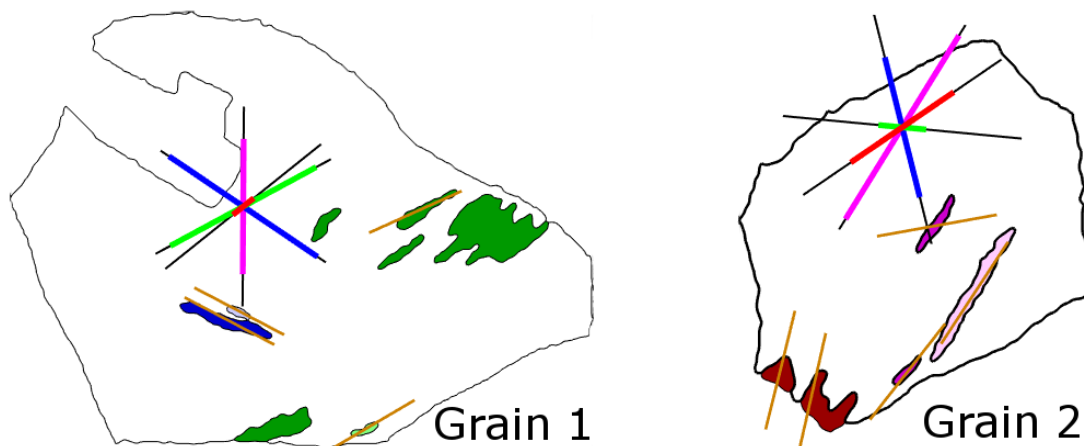

Figure 8: EBSD maps of the two grains studied. The martensite is coloured to represent the different K-S variants (see Figure 4). The {111} austenite slip traces of these different variants are shown, where the length of the coloured line is proportional to the Schmid factor. The strain-induced martensite plates display the (110) slip line trace, indicating that the K-S orientation relationship is approximately observed.

It is observed that the orientation relationship between austenite and strain-induced martensite approximately follows the K-S relationship. These martensite plates form in austenite grains along the {111} slip planes with higher Schmid factors. In grain 1 it is seen that the martensite forms along the corresponding slip line traces, and these seem to be the dominant slip systems active within the grain. In grain 2, however, although the pink coloured martensite variant occurs along the active slip plane, the red coloured variants do not have an ideal match. This mismatch may be due to the constraints provided by the surrounding grains. Kundu *et al.* [23] modelled transformation texture in austenite grains of having Goss and Cube components of texture that showed martensite variant selection. As explained earlier the model was based on the interaction of the applied stress with the shape deformation associated with the martensitic phase change and interaction energy calculated in accordance with Patel *et al.* [22]. We have applied this model to our data as shown in figure 9.
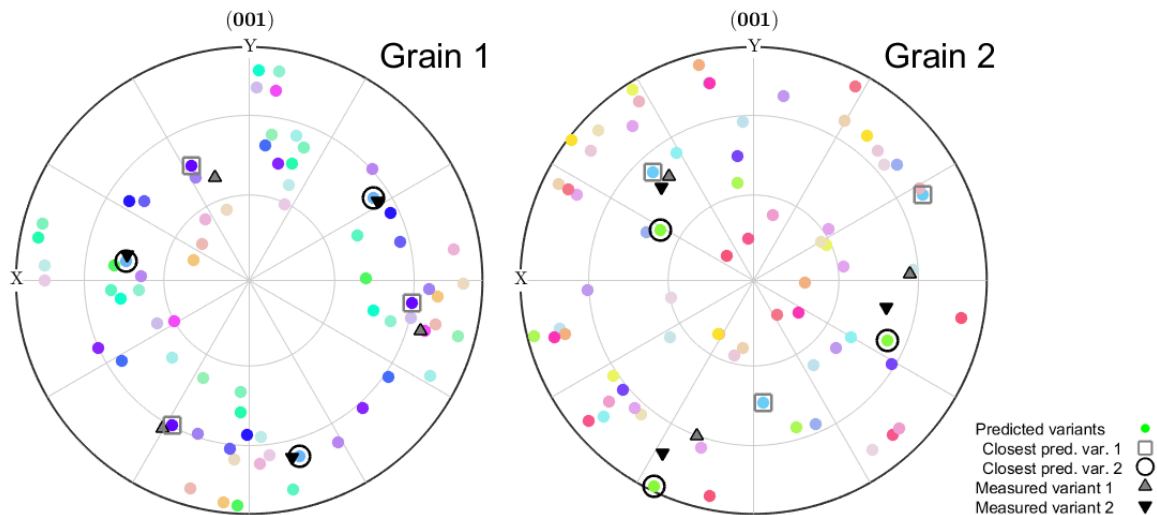
Figure 9: Pole figure plots of the spread of 24 possible martensite variants predicted for grain 1 and grain 2. The coloured circle is predictions, the triangles are the measured variants and the circle encircling the predictions shows the closest match for a given grain.

In Figure 9 all the predicted martensite variants based on the above model for grain 1 and grain 2 are shown. In grain 1, the measured variant 2 is the closest to the predicted variants, which is ranked third in the list of 24 possible variants based on interaction energy [22], [23]. Hence, for this variant there is a good agreement between the predicted and measured variants. However, the same was not true for grain 2; the agreement between the predicted and measured variants was poor and the closest to the measured variant was variant 13, which is ranked eighth out of 24 possible variants. In grain 2, martensite transformation occurs on the {111} slip plane with the highest critically-resolved shear stress (highest Schmid factor). Here, it is thought that the nucleation site is on highly deformed shear bands. These are locations of planar defects arising from the overlapping of stacking faults on the {111} austenite slip planes [34].

From Figure 10 it is shown that there is also a correlation between the maximum Schmid factor and the number of strain-induced martensite variants formed within a single grain. As shown earlier, slip bands mostly form on {111} slip systems with the highest Schmid factor. Furthermore, the martensite also tends to form along these slip bands. An example of this is shown in figure 8, but this is also found in several more grains (see figure 10 (B)). For an austenite grain having a single dominant slip system, slip is limited to a single slip plane and direction and strain-induced martensite appears to form mainly along this plane (grain 2 and 4); whereas if a single dominant slip system is not observed, with two slip systems having a similar critically-resolved shear stress, martensite nucleation can occur on both the slip planes (grain 1 and 3), meaning a greater number of martensite orientations are present in that particular grain. It is thought that the sequence of transformation has the following steps [34], [51], [52]:

- Dislocation generation, accumulation and glide along the {111} slip systems with highest critically resolved shear stress. Slip lines occur when critically-resolved shear stress crosses its threshold, enabling the slip system to get activated.

- Formation of nucleation sites (martensite embryos) – i.e. locations of planar defects – arises from overlapping of stacking faults; they may also form at the intersection of the shear bands.

- Further deformation of the austenite grains with nucleation sites leads to formation of strain induced α' martensite.

If the above assumptions are correct, the use of the Schmid factor (see figure 10 (A)) to predict the number of variants forming within a single austenite grain can offer some insight, as can be seen from figure 10 (B). For example, grains with very low Schmid factor (numbered 5 and 6) have little transformation present, and grains with moderate to high Schmid factor (numbered 1 to 4) may have up to 8 variants present. However, because some grains with moderate Schmid factor have 2 active slip systems and therefore the opportunity for many more variants to form, Schmid factor alone does not give the full picture. Some grains with the highest Schmid factor show no sign of transformation at all, this could be due to the 2 dimensional cross-section of a 3 dimensional system. The summarized data for the 6 sampled grains from figure 10b is summarized in table 4.
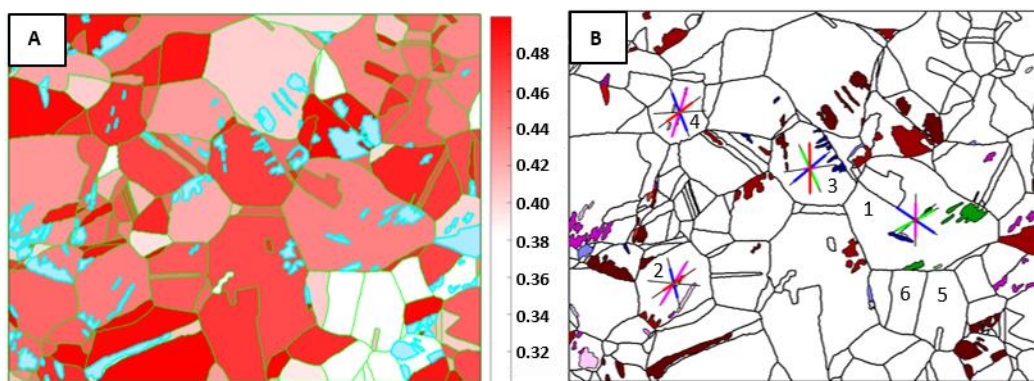

Figure 10*: Figure (A) Schmid factor map of austenite grains at 10 % strain with the martensite phase shown in blue (B) Strain-induced martensite variants at 10 % global strain within each of these austenite grains. The {111} austenite slip traces of these different variants are shown for Grains 1 to Grain 4, where the length of the coloured line is proportional to the critically-resolved shear stress on that plane.*

Table 4. List of Schmid factor, number of active slip systems, and number of strain induced martensite variants

Grain number	Schmid factor	No. of active slip systems	No. of variants
1	0.44	2	8
2	0.45	1	5
3	0.47	2	8
4	0.48	1	4
5	0.38	0	0
6	0.37	0	0

In order to improve the ability to predict transformation in each austenite grain, further work is needed to explore plasticity prior to transformation using more complicated plasticity models. It is observed that within a grain there are often multiple slip systems active, which would not be considered using the Sachs model [53]. In this model the stress state of each grain is assumed to be the same, and the active slip system is the one with the maximum Schmid factor. A good first approximation to account for this is to assume all grains have the same strain, as used in the Taylor model [54], [55]; however with the data we have available by combining local strain measurements with EBSD, this is also an unreasonable assumption. For the meantime, using Schmid factor as a first approximation is felt to be the most reasonable method considering the experimental rather than modelling scope of this work.

5. Conclusions

In this work, strain-induced martensitic transformations in TRIP steel have been studied by *in situ* EBSD and high resolution digital image correlation to better understand the mechanisms and conditions of the strain-induced martensitic transformations. The main conclusions of this work are as follows:

- Combining high-resolution DIC (HR-DIC) with EBSD has proven invaluable understanding for the crystallographic origins of local strains owing to plastic deformation and phase transformations in polycrystalline steel.

- The variant selection model of Kundu *et al.* predicts the transformation only in some grains: where it fails is possibly due to the constraints provided by the surrounding material. A more robust technique needs to be developed that can incorporate these effects.

- Upon straining, plastic deformation occurs due to the formation of {111} slip bands. Subsequent deformation of the austenite leads to strain-induced martensitic phase transformation. These martensite plates form along the {111} slip planes in the deformed austenite grains with the $(111)_\gamma$ parallel to $(0.012886\ 0.981915\ 0.978457)_{\alpha'}$, and the $[110]_\gamma$ direction parallel $[0.927033\ 1.055684\ -1.071623]_{\alpha'}$ [44]; however, the K-S orientation relationship is found to be a good approximation.

- The Schmid factor has been shown to be a useful method to predict if transformation will occur in a particular grain, however it is limited in predicting the number of variants due to not taking into account slip on multiple slip systems.

- Combining DIC examination with EBSD has confirmed that grains containing two slip systems with high and similar Schmid factors show slip in two directions and independently corroborates the conclusion that transformation occurs along these slip lines.

6. Acknowledgement

References

[1]   M. Takahashi, "Development of high strength steels for automobiles," *Shinnittetsu Giho*, no. 88, pp. 2–7, 2003.

[2]   R. J. Moat, S. Y. Zhang, J. Kelleher, a. F. Mark, T. Mori, and P. J. Withers, "Work hardening induced by martensite during transformation-induced plasticity in plain carbon steel," *Acta Mater.*, vol. 60, no. 20, pp. 6931–6939, Dec. 2012.

[3]   G. Olson and M. Cohen, "Stress-assisted isothermal martensitic transformation: application to TRIP steels," *Metall. Trans. A*, vol. 13, no. November, pp. 1907–1914, 1982.

[4]   J. Talonen, "Effect Strain-Induced α'-Martensite Transformation on Mechanical Properties of Metastable Austenitic Stainless Steels," Helsinki University of Technology, 2007.

[5]   F. Lecroisey and A. Pineau, "Martensitic transformations induced by plastic deformation in the Fe-Ni-Cr-C system," *Metall. Trans.*, vol. 3, no. 2, pp. 391–400, Feb. 1972.

[6]   E. C. Bain and N. Y. Dunkirk, "The nature of martensite," *trans. AIME*, vol. 70, no. 1, pp. 25–47, 1924.

[7]   F. . Frank, "Martensite," *Acta Metall.*, vol. 1, no. 1, pp. 15–21, Jan. 1953.

[8]   G. F. Bolling and R. H. Richman, "The plastic deformation of ferromagnetic face-centred cubic Fe-Ni-C alloys," *Philos. Mag.*, vol. 19, no. 158, pp. 247–264, Feb. 1969.

[9]   F. Delogu, "A few details of the austenite to martensite phase transformation in 304 stainless steel powders under mechanical processing," *Acta Mater.*, vol. 59, no. 5, pp. 2069–2074, Mar. 2011.

[10]   N. Tsuchida, Y. Yamaguchi, Y. Morimoto, T. Tonan, and Y. Takagi, "Effects of Temperature and Strain Rate on TRIP Effect in SUS301L Metastable Austenitic Stainless Steel," *ISIJ Int.*, vol. 53, no. 10, pp. 1881–1887, 2013.

[11]   V. Zackay, E. Parker, D. Fahr, and R. Busch, "The enhancement of ductility in high-strength steels," *ASM Trans Quart*, 1967.

[12]   H. K. D. H. Bhadeshia, "TRIP-Assisted Steels?," *ISIJ Int.*, vol. 42, no. 9, pp. 1059–1060, 2002.

[13]   M. Cherkaoui, M. Berveiller, and X. Lemoine, "Couplings between plasticity and martensitic

phase transformation: overall behavior of polycrystalline TRIP steels," *Int. J. Plast.*, vol. 16, no. 10–11, pp. 1215–1241, Jan. 2000.

[14] N. Tsuchida, Y. Morimoto, T. Tonan, Y. Shibata, K. Fukaura, and R. Ueji, "Stress-Induced Martensitic Transformation Behaviors at Various Temperatures and Their TRIP Effects in SUS304 Metastable Austenitic Stainless Steel," *ISIJ Int.*, vol. 51, no. 1, pp. 124–129, 2011.

[15] G. Olson and M. Cohen, "Kinetics of strain-induced martensitic nucleation," *Metall. Trans. A*, vol. 6A, pp. 791–795, 1975.

[16] H. J. M. Geijselaers and E. S. Perdahcıoğlu, "Mechanically induced martensitic transformation as a stress-driven process," *Scr. Mater.*, vol. 60, no. 1, pp. 29–31, Jan. 2009.

[17] F. Roters, P. Eisenlohr, L. Hantcherli, D. D. Tjahjanto, T. R. Bieler, and D. Raabe, "Overview of constitutive laws, kinematics, homogenization and multiscale methods in crystal plasticity finite-element modeling: Theory, experiments, applications," *Acta Mater.*, vol. 58, no. 4, pp. 1152–1211, 2010.

[18] E. Cakmak, H. Choo, K. An, and Y. Ren, "A synchrotron X-ray diffraction study on the phase transformation kinetics and texture evolution of a TRIP steel subjected to torsional loading," *Acta Mater.*, vol. 60, no. 19, pp. 6703–6713, Nov. 2012.

[19] S. Chatterjee and H. K. D. H. Bhadeshia, "Transformation induced plasticity assisted steels: stress or strain affected martensitic transformation?," *Mater. Sci. Technol.*, vol. 23, no. 9, pp. 1101–1104, Sep. 2007.

[20] J. R. C. Guimarães, "Stress assisted martensite: Pre-strain, grain-size and strain-rate effects," *Mater. Sci. Eng. A*, vol. 475, no. 1–2, pp. 343–347, Feb. 2008.

[21] H. K. Yeddu, A. Borgenstam, and J. Ågren, "Stress-assisted martensitic transformations in steels: A 3-D phase-field study," *Acta Mater.*, vol. 61, no. 7, pp. 2595–2606, Apr. 2013.

[22] J. R. Patel and M. Cohen, "Criterion for the action of applied stress in the martensitic transformation," *Acta Metall.*, vol. 1, no. 5, pp. 531–538, Sep. 1953.

[23] S. Kundu and H. K. D. H. Bhadeshia, "Transformation texture in deformed stainless steel," *Scr. Mater.*, vol. 55, no. 9, pp. 779–781, Nov. 2006.

[24] H. Ferreira, G. De Abreu, S. Santana, D. Carvalho, P. Maria, D. O. Silva, S. Souto, and M. Tavares, "Deformation Induced Martensite in an AISI 301LN Stainless Steel : Characterization and Influence on Pitting Corrosion Resistance," vol. 10, no. 4, pp. 359–366, 2007.

[25] H. Abreu and M. Silva, "Texture analysis of deformation induced martensite in an AISI 301L stainless steel: microtexture and macrotexture aspects," *Mater. …*, vol. 12, no. 3, pp. 291–297, 2009.

[26] S. Kundu, "Transformation Strain and Crystallographic Texture in Steels," University of Cambridge, 2007.

[27] S. Kundu, K. Hase, and H. K. D. H. Bhadeshia, "Crystallographic texture of stress-affected bainite," *Proc. R. Soc. A Math. Phys. Eng. Sci.*, vol. 463, no. 2085, pp. 2309–2328, Sep. 2007.

[28] F. Gioacchino and J. Quinta da Fonseca, "Plastic Strain Mapping with Sub-micron Resolution Using Digital Image Correlation," *Exp. Mech.*, vol. 53, no. 5, pp. 743–754, Oct. 2012.

[29] M. D. McMurtrey, G. S. Was, B. Cui, I. Robertson, L. Smith, and D. Farkas, "Strain localization at dislocation channel-grain boundary intersections in irradiated stainless steel," *Int. J. Plast.*, vol. 56, pp. 219–231, 2014.

[30] C. C. Tasan, J. P. M. Hoefnagels, M. Diehl, D. Yan, F. Roters, and D. Raabe, "Strain localization and damage in dual phase steels investigated by coupled in-situ deformation experiments and crystal plasticity simulations," *Int. J. Plast.*, vol. 63, pp. 198–210, 2014.

[31] H. Lim, J. D. Carroll, C. C. Battaile, T. E. Buchheit, B. L. Boyce, and C. R. Weinberger, "Grain-scale experimental validation of crystal plasticity finite element simulations of tantalum oligocrystals," *Int. J. Plast.*, vol. 60, pp. 1–18, 2014.

[32] F. Di Gioacchino and J. Q. da Fonseca, "An experimental study of the polycrystalline plasticity of austenitic stainless steel," *Int. J. Plast.*, no. July, 2015.

[33] T. H. Simm, "The use of EBSD and Digital Image Correlation to understand the deformation of HCP alloys," University of Manchester, 2007.

[34] J. Talonen and H. Hänninen, "Formation of shear bands and strain-induced martensite during plastic deformation of metastable austenitic stainless steels," *Acta Mater.*, vol. 55, no. 18, pp. 6108–6118, Oct. 2007.

[35] F. Bachmann, R. Hielscher, and H. Schaeben, "Grain detection from 2d and 3d EBSD data-Specification of the MTEX algorithm," *Ultramicroscopy*, vol. 111, no. 12, pp. 1720–1733, 2011.

[36] LaVision, *StrainMaster 8.2*. Goettingen, 2014.

[37] H. Schreier, J.-J. Orteu, and M. A. Sutton, *Image Correlation for Shape, Motion and Deformation Measurements*. Boston, MA: Springer US, 2009.

[38] B. D. Lucas and T. Kanade, "An iterative image registration technique with an application to stereo vision," *7th international joint conference on Artificial intelligence*, vol. 2. pp. 674–679, 1981.

[39] J.-Y. Bouguet, "Pyramidal implementation of the affine lucas kanade feature tracker— description of the algorithm," *Pages.Slc.Edu*, vol. 2, p. 3, 2001.

[40] W. F. Clocksin, K. F. Chivers, P. H. S. Torr, J. Quinta da Fonseca, and P. J. Withers, "Inspection of surface strain in materials using dense displacement fields," *Proc. Int. Conf. New Challenges Mesomech. Aaalborg Univ. Denmark*, vol. 2, pp. 467–475, 2002.

[41] G. Kurdjumov and G. Sachs, "Over the mechanisms of steel hardening," *Z. Phys*, vol. 64, pp. 325–343, 1930.

[42] J. . Bowles and J. . Mackenzie, "The crystallography of martensite transformations I," *Acta Metall.*, vol. 2, no. 1, pp. 129–137, Jan. 1954.

[43] J. . Mackenzie and J. . Bowles, "The crystallography of martensite transformations II," *Acta Metall.*, vol. 2, no. 1, pp. 138–147, Jan. 1954.

[44] H. Bhadeshia, "Worked Examples in the Geometry of Crystals', 1987," *London, Inst. Met.*

[45] T. H. Simm, Y. Das, L. Sun, M. Williams, Y. Li, M. E. Fitzpatrick, S. Gungor, P. Hill, H. K. D. H. Bhadeshia, R. J. Moat, M. Rawson, and Prakas, "dbsd and dice : Open-Source EBSD and Digital Image Correlation Software for Analysing Steels," *Unpubl. Work*, 2016.

[46] H. Kato, R. Moat, T. Mori, K. Sasaki, and P. Withers, "Back Stress Work Hardening Confirmed by Bauschinger Effect in a TRIP Steel Using Bending Tests," vol. 54, no. 7, pp. 1715–1718, 2014.

[47] M. a. Sutton, N. Li, D. C. Joy, a. P. Reynolds, and X. Li, "Scanning Electron Microscopy for

Quantitative Small and Large Deformation Measurements Part I: SEM Imaging at Magnifications from 200 to 10,000," *Exp. Mech.*, vol. 47, no. 6, pp. 775–787, Mar. 2007.

[48]   G. Dieter, "Mechanical metallurgy," 2015.

[49]   A. D. Kammers and S. Daly, "Digital Image Correlation under Scanning Electron Microscopy: Methodology and Validation," *Exp. Mech.*, vol. 53, no. 9, pp. 1743–1761, 2013.

[50]   L. Patriarca, W. Abuzaid, H. Sehitoglu, and H. J. Maier, "Slip transmission in bcc FeCr polycrystal," *Mater. Sci. Eng. A*, vol. 588, pp. 308–317, 2013.

[51]   G. B. Olson and M. Cohen, "A mechanism for the strain-induced martensitic transformations," *J. Less-Common Met.*, vol. 28, pp. 107–118, 1972.

[52]   N. Gey, B. Petit, and M. Humbert, "Electron backscattered diffraction study of ε/α' martensitic variants induced by plastic deformation in 304 stainless steel," *Metall. Mater. Trans. A*, vol. 36, no. December, 2005.

[53]   G. Sachs, "Zur Ableitung einer FlieBbedingung," *Z. Ver. Deu. Ing*, vol. 72, no. 22, p. 734, 1928.

[54]   H. J. Bunge, "Some applications of the Taylor theory of polycrystal plasticity," *Krist. und Tech.*, vol. 5, no. 1, pp. 145–175, 1970.

[55]   G. L. Taylor, "Plastic strain in metals," *J. Inst. Met.*, vol. 62, p. 307, 1938.